RSC Advances

PAPER

View Article Online
View Journal | View Issue

Cite this: *RSC Adv.*, 2022, **12**, 17919

Ag@ZIF-8/g-C_3N_4 Z-scheme photocatalyst for the enhanced removal of multiple classes of antibiotics by integrated adsorption and photocatalytic degradation under visible light irradiation†

Xin Guo,‡ Siyuan He,‡ Zhe Meng, * Yinghui Wang and Yuan Peng

By combining the plasmon resonance of Ag nanoparticles and orientation effects of ZIF-8, as well as the visible-light activity of g-C_3N_4, we constructed a direct Z-scheme heterojunction with a co-existing Ag^+/Ag^0 system by an *in situ* coprecipitation method. The presence of Ag^+/Ag^0 on the surface of ZIF-8 was confirmed by the exchange of Ag^+ and Zn^{2+} ions. This promoted the reduction of the band gap of ZIF-8, according to X-ray diffraction (XRD) and X-ray photoelectron spectroscopy. The results reveal that the 12 wt% Ag@ZIF-8/g-C_3N_4 nanocomposite presented the best adsorptive–photocatalytic activity for the degradation of multi-residue antibiotics under visible light irradiation for 60 min. Its degradation efficiency reached 90%, and its average apparent reaction rate constant was 10.27 times that of pure g-C_3N_4. In the radical scavenger experiments, $^{\bullet}O_2^-$ and $^{\bullet}OH$ were shown to be important in the process of photocatalytic degradation. In addition, we proposed a possible direct Z-scheme photocatalytic mechanism, that is, an internal electric field was formed to compensate the mediators between the interfaces of Ag@ZIF-8 and g-C_3N_4. This improvement can be attributed to the direct Z-scheme heterojunction system fabricated between Ag@ZIF-8 and g-C_3N_4. This can accelerate photogenerated electron–hole separation and the redox capability of Ag@ZIF-8/g-C_3N_4. The integration of the adsorption and photocatalytic degradation of various antibiotics is a promising approach. ZIF-8 has been widely used in the integrated adsorptive–photocatalytic removal of various antibiotics due to its large surface area, high orientation adsorption capacity. Therefore, this study provides new insights into the design of enhanced redox capacity for the efficient degradation of multiple antibiotics under visible-light irradiation.

Received 5th April 2022
Accepted 12th May 2022

DOI: 10.1039/d2ra02194c

rsc.li/rsc-advances

1. Introduction

The problem of antibiotic pollution in water is becoming more and more serious and has attracted widespread attention. Some antibiotics, such as sulfonamides, tetracyclines, and fluoroquinolones, are widely used in the treatment of infectious diseases of human and animals. In addition, they are added to feed in animal husbandry and aquaculture to promote animal growth and development.[1,2] Moreover, antibiotic residues in environmental water have a long half-life. This not only affects the activity of organisms but also harms human health by entering the food chain. Therefore, research on the effective removal of various antibiotics in environmental water has gained public focus and needs to be urgently solved. Currently, semiconductor-based photocatalytic technology has been considered as one of the promising routes to solve the degradation of organics pollutants in environmental water. Photocatalysts have great potential to convert light energy into chemical energy to decompose various harmful antibiotic contaminants.[3–5] However, there are few literature reports on the simultaneous removal of multiple classes of antibiotic residues by photocatalysis.

The two-dimensional (2D) graphitic-C_3N_4 (g-C_3N_4) semiconductor has a wide range of applications in the environmental and energy fields because of its visible-light activity, unique physicochemical properties, excellent chemical stability and low-cost.[6,7] Some important limitations of the photocatalytic activity of g-C_3N_4 are its low specific surface area, fast recombination of electrons and holes and poor visible light absorption.[8,9] To improve the above problems, the construction of a heterojunction with a suitable band gap semiconductor (co-catalyst) has been shown to be a good strategy to improve the

State Key Laboratory of High-efficiency Utilization of Coal and Green Chemical Engineering, National Demonstration Center for Experimental Chemistry Education, College of Chemistry and Chemical Engineering, Ningxia University, Yinchuan 750021, China. E-mail: meng_z@nxu.edu.cn; Fax: +86 951 2061231; Tel: +86 951 2061224

† Electronic supplementary information (ESI) available. See https://doi.org/10.1039/d2ra02194c

‡ These authors contributed equally.

photocatalytic performance of g-C_3N_4, such as g-C_3N_4-based conventional type II heterostructures, g-C_3N_4-based Z-scheme heterostructures, and g-C_3N_4-based p–n heterostructures, *etc.* The unique "Z" shape as the transport pathway of photo-generated charge carriers in Z-scheme photocatalytic systems is the most similar system to mimic natural photosynthesis in the many g-C_3N_4-based heterojunction photocatalysts. The construction of Z-scheme photocatalytic systems can promote visible light utilization and carrier separation, and maintain the strong reducibility and oxidizability of semiconductors.[10–14] There are many studies on g-C_3N_4-based Z-scheme heterojunction photocatalysts, such as ZnO/g-C_3N_4,[15,16] g-C_3N_4/ZnS,[17] g-C_3N_4/graphene/$NiFe_2O_4$,[18] NiCo/ZnO/g-C_3N_4,[19] $Bi_2Zr_2O_7$/g-C_3N_4/Ag_3PO_4,[20] g-C_3N_4/$NiFe_2O_4$,[21] and WO_3/g-C_3N_4 [22] and *etc.* These Z-scheme heterojunction photocatalysts have been made to improve the photocatalytic activity by combining with other semiconductor materials. However, there are some problems with the single photocatalytic method, such as low adsorption ability, limited active sites and low removal efficiency. The integration of the adsorption and photocatalytic degradation of various organic pollutants is considered as a suitable and promising technology. Therefore, it is still essential to fabricate photocatalysts with superior adsorption and degradation efficiencies.

Metal–organic zeolitic imidazolate frameworks (ZIFs) are a kind of porous organic/inorganic hybrid material that forms a 3D tetrahedral framework. It is well known that ZIF-8 has the advantages of a high surface area, high crystallinity and numerous active sites on the surface. It has been intensively studied and widely used in adsorption and photocatalytic systems.[23–25] ZIF-8, composed of the metal ions Zn^{2+} and 2-methylimidazole, is a typical member of the ZIF family.[26] Compared with pure ZIF-8, our previous research proved that ZIF-8-based composite (ZIF-8@graphene) had a superior selective adsorption capacity for trace antibiotics in wastewater.[27] However, ZIF-8 always has some disadvantages. For example, ZIF-8 shows barely photocatalytic activity under visible light irradiation because of its large band gap (E_g = 5.0).[28] One strategy that can further improve the photocatalytic activity of ZIF-8 is to incorporate light-harvesting noble-metal nanoparticles in ZIF-8. The noble-metal with plasmonic nanostructures (Au and Ag nanoparticles) can control resonant photons and induce coherent conduction band electron oscillation.[29,30] More and more attention has been paid to the localized surface plasmon resonance (LSPR), especially in the field of catalysis. Chang *et al.* reported that Ag encapsulated in ZIF-8 can help to create surface plasmon resonance on ZIF-8 nanocrystals.[31] This approach not only expands the visible light absorption, but also further reduces the band gap. The band gap energy (E_g) of Ag@ZIF-8 nanohybrids is narrower than that of ZIF-8. This can effectively inhibit the recombination rate of the charge carriers (photogenerated electron–hole pairs) of bare porous ZIF-8 nanomaterials. Fan *et al.* reported that the photocatalytic activity of a nanocomposite made of Ag/AgCl@ZIF-8 was better than that of the bare Ag/AgCl photocatalyst.[32] Since Ag@ZIF-8 nanoparticles are easy to aggregate in water, this leads to a reduction in their adsorption–photocatalysis performance.

Integrating Ag@ZIF-8, with orientation adsorption effects, and g-C_3N_4, with visible-light activity, is a very good and viable strategy for the selective degradation of multiple antibiotics under visible light irradiation. Coupling Ag@ZIF-8 on g-C_3N_4 can introduce multiple benefits: (1) providing numerous selective adsorption sites, (2) distributing and stabilizing the photocatalyst nanoparticles and (3) improving the photo-generated charge transfer process *via* the unique electronic properties of its direct Z-scheme. However, no study has used a direct Z-scheme heterogeneous system to improve the separation efficiency of carriers by encapsulating Ag nanoparticles into ZIF-8, and then coupling with graphitic-C_3N_4 to form a Ag@ZIF-8/g-C_3N_4 heterostructure.

In this paper, nanoparticles of the noble metal Ag were encapsulated into zeolitic imidazolate framework-8 to form a new composite Ag@ZIF-8 with two types of coexisting Ag species (Ag^0 and Ag^+) through a simple *in situ* self-assembly process. The visible light-driven Ag@ZIF-8/g-C_3N_4 photocatalysts exhibit superior photocatalytic performances. 12 wt% Ag@ZIF-8/g-C_3N_4 shows the highest degradation efficiency of 90% of various antibiotics from water within 60 min under visible light irradiation. On the basis of the detailed experimental analysis, a direct Z-scheme mechanism was proposed to enhance the photocatalytic behaviors of Ag@ZIF-8/g-C_3N_4 composites.

2. Experimental

2.1 Synthesis of Ag@ZIF-8/g-C_3N_4 photocatalysts

The synthesis of the composite photocatalyst is shown in Scheme 1. g-C_3N_4 was synthesized through thermal polycondensation with programmed temperatures. Melamine was calcinated in a quartz crucible with a cover, and placed in a tube furnace with quartz tubes. The program settings of the calcination temperature were: the initial temperature was 200 °C for 20 min. After that, it was heated at a rate of 2 °C min^{-1} to 350 °C for 90 min. Finally, it was heated at a rate of 2 °C min^{-1} to 550 °C for 120 min.

Nanoscale ZIF-8 was prepared by the co-precipitation method. In the synthesis of ZIF-8, 1.78 g of $Zn(NO_3)_2 \cdot 6H_2O$ and 5.26 g of 2-methylimidazole were dispersed in two beakers containing 40 ml of methanol. Then, the suspension was stirred at 30 °C for 4 h. The product was recovered by centrifugation, and washed with fresh methanol three times. Then, it was dried at 60 °C for 12 h.

The Ag@ZIF-8 hybrid was obtained by mixing ZIF-8 with $AgNO_3$. 0.20 g of ZIF-8 and 0.17 g of $AgNO_3$ were dispersed into two beakers containing 20 ml of methanol. The two components were mixed by stirring for 25 min in the dark. We centrifuged the precipitate, and washed it with fresh methanol several times. Then, it was dried at 60 °C for 12 h. We defined the samples as Ag-doped-ZIF-8 (Ag@ZIF-8) by encapsulating Ag nanoparticles into zeolitic imidazolate framework-8. According to the amount of $AgNO_3$ added, the samples of Ag@ZIF-8 were defined as 1.5 mmol, 1.0 mmol, and 0.5 mmol Ag@ZIF-8.

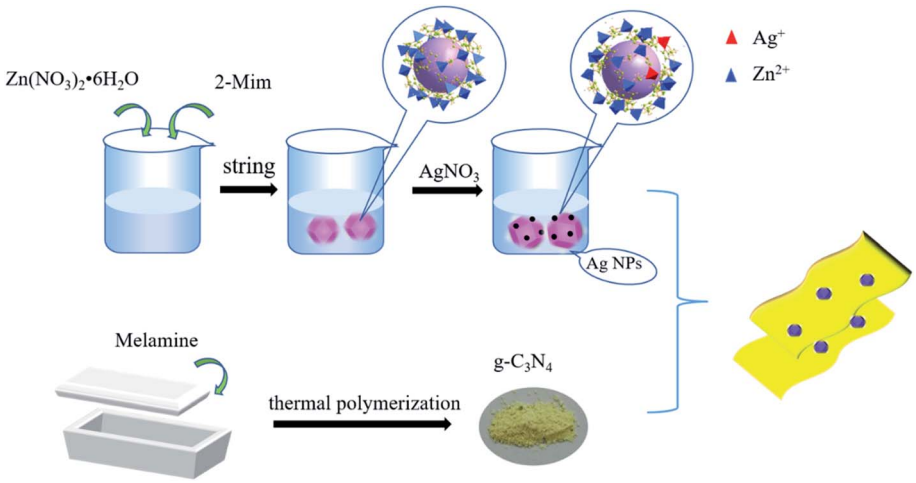

Scheme 1 Schematic illustration of the preparation of Ag@ZIF-8/g-C_3N_4.

The Ag@ZIF-8/g-C_3N_4 composites were obtained by a simple *in situ* self-assembly process at room temperature. Ag@ZIF-8 and g-C_3N_4 in a certain mass ratio were dispersed in methanol and stirred for 30 min. Finally, the obtained product was dried at 60 °C for 12 h. The Ag@ZIF-8/g-C_3N_4 heterostructures were denoted as *x* wt% Ag@ZIF-8/g-C_3N_4 (10 wt%, 12 wt%, 17 wt%, 25 wt%), where *x* represents the Ag@ZIF-8 content in the heterostructures.

2.2 Photocatalytic performance measurements

2.2.1 Photodegradation of antibiotics. The photoreactor was water-cooled and made of double-walled quartz. The photodegradation experiments of ten antibiotics were carried out under visible light irradiation. A 300 W Xe-lamp equipped with a cut-off filter (>420 nm) served as the visible light source. 20 mg of the Ag@ZIF-8/g-C_3N_4 sample was dispersed in 30 ml of a mixed solution containing ten antibiotics (pH = 9, 10 μg ml^{-1}). The reaction system was stirred for nearly 30 min in the dark before irradiation to reach the adsorption/desorption equilibrium. Then, the reaction system was continuously stirred under visible light. At specific given times during the reaction, a suspension of 0.5 ml was taken out and then filtered using a 0.22 μm filter membrane. The changes of the antibiotics' concentrations were measured by UHPLC-MS/MS.

2.2.2 Trapping experiments of active species. In the trapping experiments, we investigated radicals and holes under similar experimental conditions for the photodegradation of antibiotics. We added specific scavengers into the suspension system before visible light irradiation. Three typical scavengers (dosage: 1 mmol L^{-1}), EDTA–2Na, IPA and BQ, served as scavengers of h^+, $^{\cdot}OH$ and $^{\cdot}O_2^-$, respectively.

3. Results and discussion

3.1 Characterization of the photocatalysts

The X-ray diffraction (XRD) patterns of the synthesized samples are shown in Fig. 1(a). The two diffraction peaks of g-C_3N_4 at approximately 13.3° and 27.3° corresponded to the (110) and (002) crystal planes, respectively. These were the same as those reported.[33] In Fig. 1(a), the diffraction peaks of ZIF-8 indicated that it has the sodalite zeolite type structure. The predominant diffraction peaks (011), (002), (112), (022), (013), (222), (114), (233), (134) and (044) identified in the XRD patterns were the same as those reported.[34] Meanwhile, two strong coupling peaks were observed for the (002) and (100) planes of g-C_3N_4, combining with the (134) and (112) planes of ZIF-8 in the Ag@ZIF-8/g-C_3N_4 samples, as shown in Fig. 1(a). In Fig. 1(b), a typical diffraction peak at 8.7° was found in the Ag@ZIF-8 composite. Furthermore, with the increase of the silver content, the diffraction peak intensity (8.7°) was significantly increased. This was attributed to silver imidazolate oligomers. This is the only peak for Ag-containing phases in the XRD patterns. This is consistent with the literature.[34] The XRD diffraction peaks of ZIF-8 and Ag@ZIF-8 were amplified at the small angle range from 3° to 8° to further determine the presence of Ag-containing phases. In Fig. 1(c), the angle of the main diffraction peak of Ag@ZIF-8 was smaller than that of ZIF-8. According to the Bragg equation, $2d \sin\theta = n\lambda$, when XRD peaks shift to a smaller angle, the distance between the parallel atomic planes (*d*) has increased. The ionic radius of Ag is greater than that of Zn. The Ag ions partially replaced Zn ions in the host crystal and the diffraction peak was shifted to a smaller angle than that of ZIF-8. However, the XRD peak intensities of ZIF-8 decreased with the addition of Ag. This indicates that the localized crystalline structure was modified after Ag ions were introduced. XRD diffraction spectrum analysis showed that two Ag-containing phases were found in Ag@ZIF-8. As shown in Fig. 1(d), the FT-IR spectra of the samples were used to study the chemical functional groups of bare g-C_3N_4 and ZIF-8, and the Ag@ZIF-8/g-C_3N_4 composite. Compared with the FT-IR spectra of bare g-C_3N_4 and ZIF-8, the characteristic absorption of typical functional groups was clearly observed in the Ag@ZIF-8/g-C_3N_4 composite. For example, the absorption band at 810 cm^{-1} and the absorption peak at 421 cm^{-1} resulted from the plane repeating arrangement of the tri-*s*-triazine rings for g-C_3N_4 and

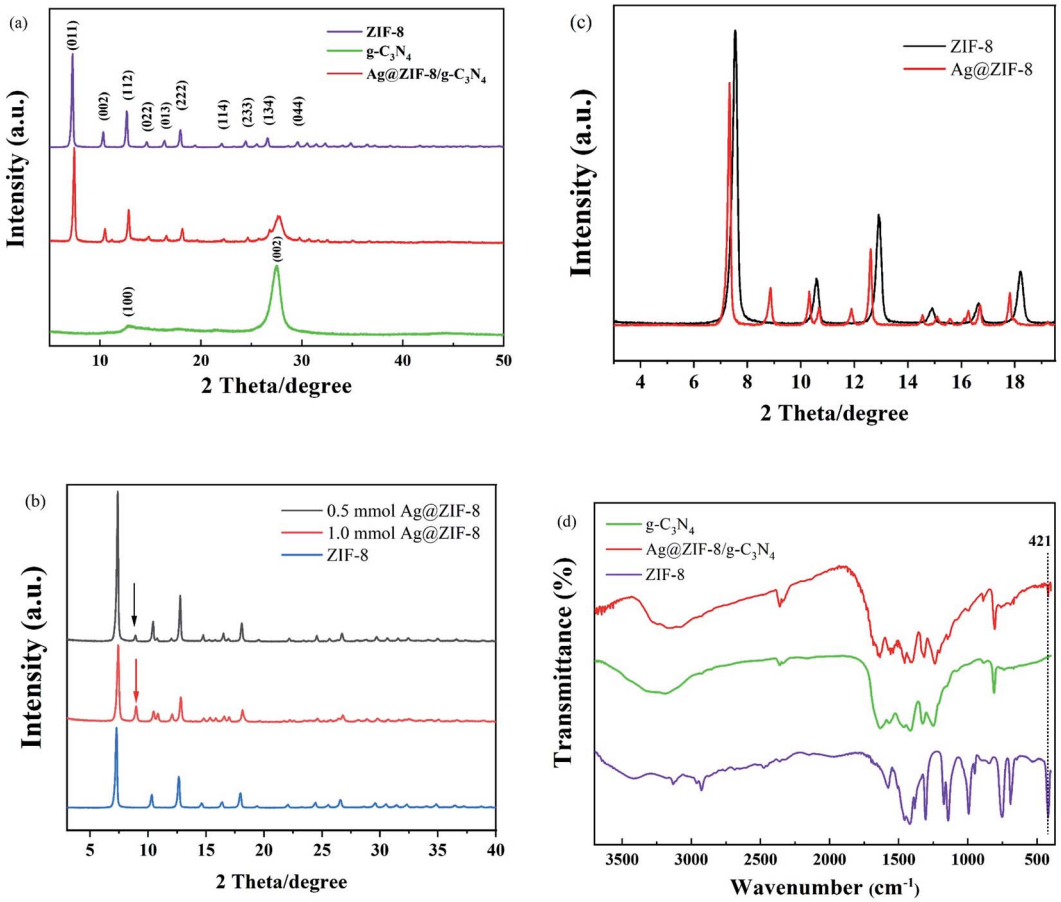

Fig. 1 XRD patterns of (a) ZIF-8, g-C_3N_4 and Ag@ZIF-8/g-C_3N_4, (b) ZIF-8 and Ag@ZIF-8 with different Ag contents and (c) enlarged view of ZIF-8 and Ag@ZIF-8. (d) FT-IR spectra of Ag@ZIF-8, g-C_3N_4 and Ag@ZIF-8/g-C_3N_4.

the Zn–N stretching vibration for ZIF-8, respectively. No impurity peaks were observed in the Ag@ZIF-8/g-C_3N_4 composite.

The morphological features and nanoparticle size distributions of the obtained Ag@ZIF-8 (1 mmol $AgNO_3$) and 12 wt% Ag@ZIF-8/g-C_3N_4 composites were evaluated by SEM imaging. As shown in Fig. 2(a), Ag nanoparticles with a diameter of 10 nm were uniformly distributed on the surface of ZIF-8 with a dodecahedral structure (about 180 nm) by loading 1 mmol of silver ($AgNO_3$). Compared with the pure ZIF-8 shown in Fig. 2(a), each crystal face of the Ag@ZIF-8 nanoparticles with the dodecahedral structure showed significant shrinkage. The conclusions of SEM and XRD are consistent. This further confirmed that the silver nanoparticles were embedded into the framework of ZIFs through the stable chemical bonds between Ag and ZIF-8. Therefore, with the addition of silver nitrate solution, Ag nanoparticles were embedded into the ZIF-8 framework, and ion exchange occurred between Ag^+ in the solution and Zn^{2+} in the ZIF-8 framework. As shown in Fig. 2(b), an encouraging phenomenon was the emergence of g-C_3N_4 nanosheets in the Ag@ZIF-8/g-C_3N_4 composite, that is, contacting interfaces were formed between the g-C_3N_4 nanosheets and Ag@ZIF-8 nanoparticles.

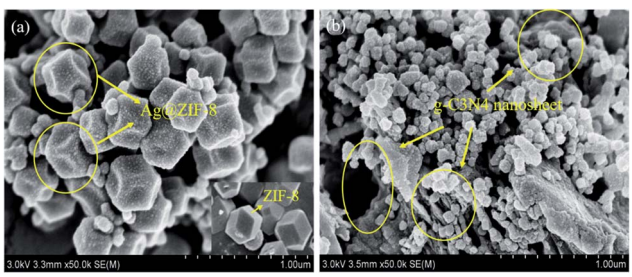

Fig. 2 SEM images of (a) Ag@ZIF-8 and (b) Ag@ZIF-8/g-C_3N_4.

We observed the morphology and composition of the 12 wt% Ag@ZIF-8/g-C_3N_4 composite by TEM and EDS. As shown in Fig. 3(a), Ag nanoparticles were uniformly dispersed and grown on the surface of ZIF-8 to form the Ag@ZIF-8 composite. Fig. 3(b) shows that Ag@ZIF-8 nanoparticles were anchored on g-C_3N_4 nanosheets to construct the Ag@ZIF-8/g-C_3N_4 composite. To further demonstrate the coexistence of Ag@ZIF-8/g-C_3N_4, HRTEM images of Ag@ZIF-8/g-C_3N_4 composites demonstrated the clear lattice fingerprints of the different species, as shown in Fig. 3(c and d). The spacings were 0.24 nm and 0.27 nm, corresponding to the (111) and (111) planes of Ag^0 and Ag^+ (Fig. 3(c)), respectively. In addition, the lattice fingerprints of g-C_3N_4 were the same as those reported in ref. 35. According to the EDX patterns in Fig. 3(e and f), C, N, Zn and Ag

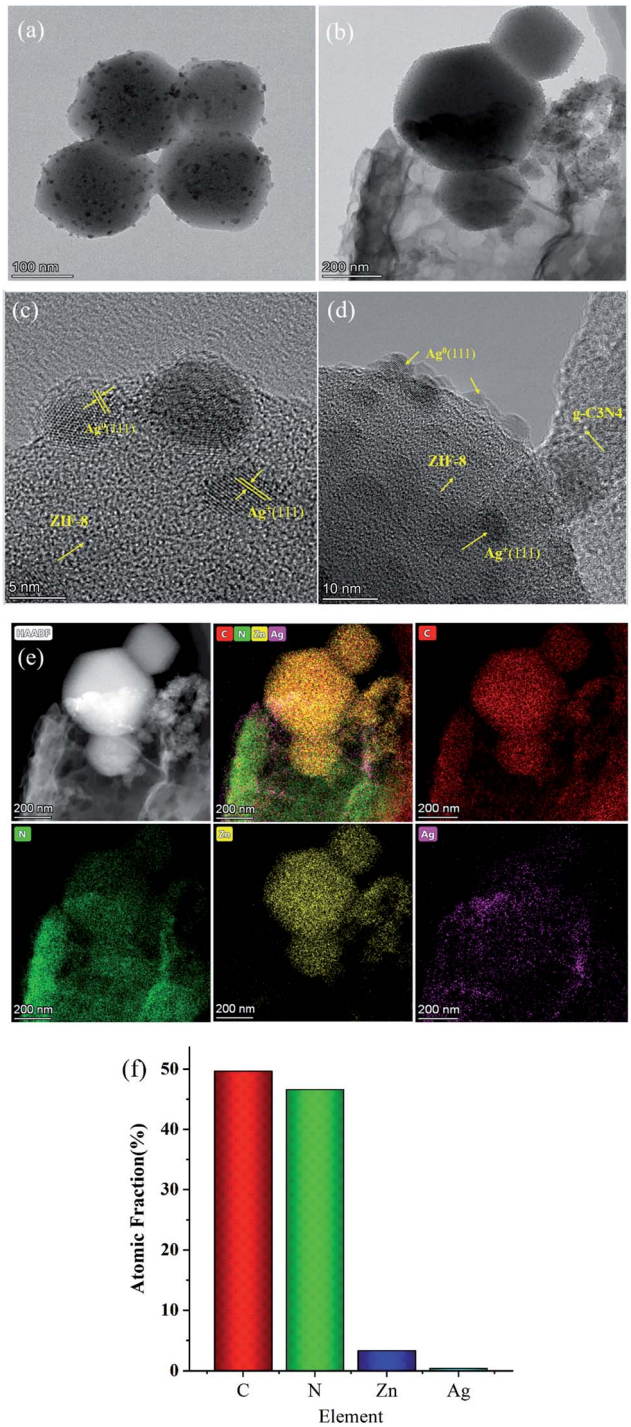

Fig. 3 TEM images of (a) Ag@ZIF-8 and (b–d) Ag@ZIF-8/g-C_3N_4, (e) EDS spectrum of Ag@ZIF-8/g-C_3N_4 and (f) atomic percentages of Ag@ZIF-8/g-C_3N_4.

were uniformly distributed in its structure. The atomic percentages of the four elements were 49.67%, 46.62%, 3.30% and 0.41%, respectively. These findings confirmed the coexistence of Ag@ZIF-8 and g-C_3N_4 in the composite. In addition, SEM, TEM and EDS data supported the XRD data. The obtained composite showed Ag nanoparticles encapsulated into the zeolitic imidazolate framework and coupled on the surface of graphitic-C_3N_4.

The specific surface areas and pore structures of the samples were obtained by the study of the N_2 adsorption–desorption isotherms. In Fig. 4(a and b), the specific surface areas of the prepared ZIF-8, Ag@ZIF-8, Ag@ZIF-8/g-C_3N_4, and pure g-C_3N_4 were evaluated through the Brunauer–Emmett–Teller (BET) method to be 492.43, 253.10, 104.51 and 5.60 $m^2\ g^{-1}$, respectively. Compared with that of pure ZIF-8, the BET of the hybrid sample Ag@ZIF-8 was decreased greatly due to the introduction of Ag^+. This verified the shrinkage of the ZIF-8 crystal plane observed in the SEM image (Fig. 4(a)). However, compared with that of bare g-C_3N_4 (5.60 $m^2\ g^{-1}$), the Ag@ZIF-8/g-C_3N_4 hybrid composite had a high BET measurement of 104.51 $m^2\ g^{-1}$, as shown in Fig. 4(b). The pore size distributions of the prepared ZIF-8, Ag@ZIF-8, Ag@ZIF-8/g-C_3N_4, and pure g-C_3N_4 were 4.05, 4.48, 6.17 and 23.23 nm, respectively. All samples showed characteristics of mesoporous structures because of the

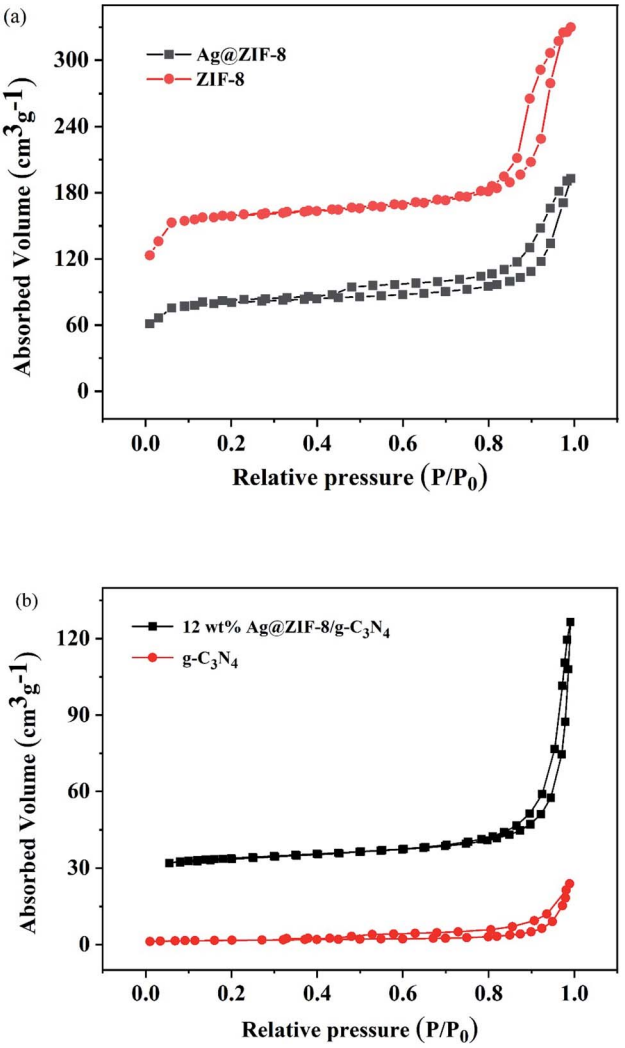

Fig. 4 Adsorption–desorption isotherms of (a) ZIF-8, Ag@ZIF-8, (b) g-C_3N_4, 12 wt% Ag@ZIF-8/g-C_3N_4.

presence of the type IV isotherms. Compared with Ag@ZIF-8, the pore sizes of Ag@ZIF-8/g-C_3N_4 were mainly distributed around 6 nm. This indicated that the mesopores were possibly intergranular pores from Ag@ZIF-8 and g-C_3N_4. The significant increase in the pore sizes benefitted from the close contact interface between Ag@ZIF-8 nanoparticles and g-C_3N_4

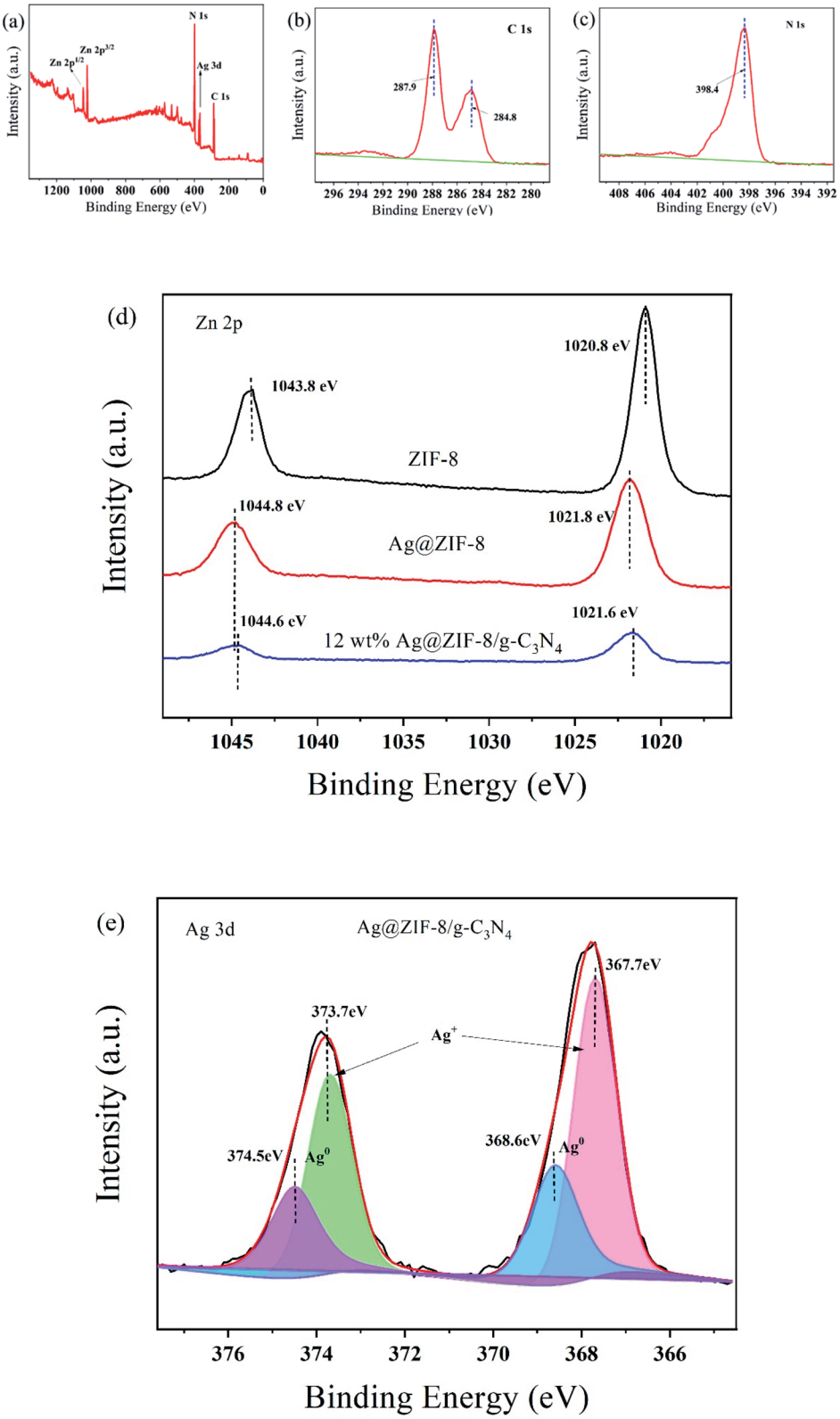

Fig. 5 XPS spectra of (a) Ag@ZIF-8/g-C_3N_4, (b) C 1s, (c) N 1s (d) Zn 2p (e) Ag 3d.

nanosheets, since the demand for an electron mediator was eliminated, and the electron and ion migration lengths were shortened, which were very conducive to building a direct Z-scheme photocatalyst.

The elemental states, surface chemical composition and electronic environment of the constituent elements of the Ag@ZIF-8/g-C_3N_4 composites were elucidated by sensitive X-ray photoelectron spectroscopy (XPS) measurements. As shown in Fig. 5(a), the XPS spectrum of the Ag@ZIF-8/g-C_3N_4 composite proves that the surface chemical composition was composed of Ag 3d, Zn 2p, N 1s and C 1s. In Fig. 5(b), two distinct peaks at 284.8 and 287.9 eV are shown in the C 1s spectrum of g-C_3N_4. This corresponds to the graphitic carbon (sp^2 C–C bonds) and the sp^2 hybridized carbon in the N-containing aromatic rings (N=C–N) of graphitic carbon nitride. In Fig. 5(c), the N 1s spectra shows a peak at 398.4 eV. This results from the bonding of sp^2 hybridized aromatic N atoms to carbon atoms (C–N=C). In Fig. 5(d), the typical high-resolution XPS signals of the Zn 2p spectra of the ZIF-8, Ag@ZIF-8, and Ag@ZIF-8/g-C_3N_4 samples are shown. The peak voltages of Zn $2p_{3/2}$ and Zn $2p_{1/2}$ were 1020.8 eV and 1043.8 eV for ZIF-8, respectively. Compared with ZIF-8 ($2p_{1/2}$, 1043.8 eV; $2p_{3/2}$, 1020.8 eV), the Zn 2p states of Ag@ZIF-8 ($2p_{1/2}$, 1044.8 eV; $2p_{3/2}$, 1021.8 eV) were shifted positively after the Ag nanoparticles were embedded into ZIF-8. This indicates that there was ion exchange between Ag^+ in the solution and Zn^{2+} in the ZIF-8 framework. Therefore, the altered Zn 2p spectra of ZIF-8 and Ag@ZIF-8 further confirmed the formation of new chemical bonds between Ag and ZIF-8. This is accordance with the previous reports.[31,36,37] In addition, there was no significant change in the Zn 2p spectra of Ag@ZIF-8 and Ag@ZIF-8/g-C_3N_4. This further confirmed the successful synthesis of the composite nanomaterials of Ag@ZIF-8 and Ag@ZIF-8/g-C_3N_4.

Additionally, we performed XPS analysis of the Ag@ZIF-8/g-C_3N_4 sample to determine the presence of Ag^+ and Ag^0 in the composite. The Ag 3d spectra are shown in Fig. 5(e). The observed Ag 3d spectrum of Ag@ZIF-8/g-C_3N_4 includes the two survey bands at 367.7 and 373.7 eV, which can be assigned to the Ag $3d_{5/2}$ and Ag $3d_{3/2}$ binding energies, respectively. However, each survey band can be further split into a pair of survey peaks (Ag $3d_{5/2}$, 367.5/368.4 eV and Ag $3d_{3/2}$, 373.5/374.1 eV).[20,38–40] The first pair of survey peaks at 367.5 and 373.5 eV was attributed to the Ag^+ of $AgNO_3$. However, the second pair of survey peaks at 368.4 and 374.1 eV resulted from the metallic Ag^0. All the XPS binding energies of Ag 3d indicated the coexistence of Ag^+ and Ag^0 phases. Such a result was consistent with

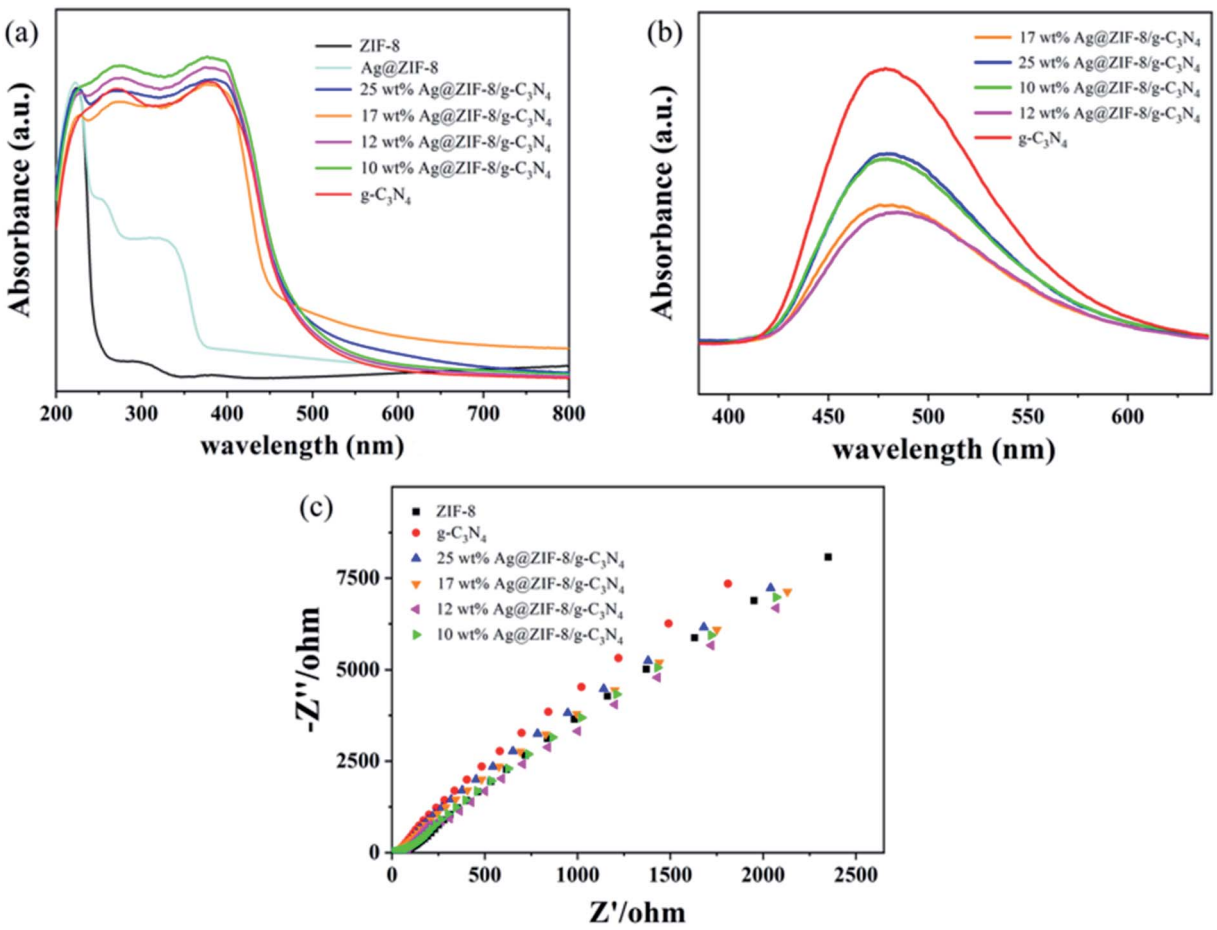

Fig. 6 (a) UV-vis diffuse reflectance spectra of pure g-C_3N_4, ZIF-8 and Ag@ZIF-8/g-C_3N_4 with different g-C_3N_4 contents, (b) PL spectra of pure g-C_3N_4 and Ag@ZIF-8/g-C_3N_4 with different g-C_3N_4 contents and (c) EIS of ZIF-8, pure g-C_3N_4 and Ag@ZIF-8/g-C_3N_4 with different g-C_3N_4 contents.

the results in the literature and the results of XRD and TEM in this work.

The UV-vis diffuse reflectance spectra of bare g-C_3N_4 and ZIF-8, as well as those of Ag@ZIF-8 and Ag@ZIF-8/g-C_3N_4 with different mass ratios of Ag/g-C_3N_4, are presented in Fig. 6(a). The bare g-C_3N_4 nanosheets and ZIF-8 nanoparticles had absorption edges at 485 and 245 nm, which corresponded to band gaps of 2.61 and 4.90 eV, respectively. Compared with that of ZIF-8, the absorption band edge of Ag@ZIF-8 was significantly red-shifted to 380 nm. This indicates that Ag doping can enhance light absorption because of the LSPR effect of plasmonic metal nanoparticles. Compared with that of the bare g-C_3N_4, the band gaps of 10 wt%, 12 wt%, 17 wt% and 25 wt% Ag@ZIF-8/g-C_3N_4 were 2.58, 2.60, 2.69 and 2.59 eV, respectively. Obviously, we could adjust the ratio of g-C_3N_4 and Ag to enhance the ability to harvest visible light.

The recombination of the photogenerated electrons and holes was shown in the photoluminescence (PL) spectra. As shown in Fig. 6(b), compared to that of g-C_3N_4, the PL intensity of 12 wt% Ag@ZIF-8/g-C_3N_4 was the lowest. This further indicated that the recombination efficiency of photogenerated carriers was low. Therefore, an appropriate Ag/g-C_3N_4 ratio could effectively inhibit the rapid recombination of photogenerated electrons and holes (e^-–h^+) in the Ag@ZIF-8/g-C_3N_4 heterostructured composite. This would be beneficial to improving the photocatalytic performance.

In order to study the photoelectric separation and the charge migration efficiency of the prepared samples, we performed electrochemical impedance spectroscopy (EIS) analysis to measure the different mass ratios of bare g-C_3N_4, ZIF-8 and the Ag@ZIF-8/g-C_3N_4 composite. Generally, the smaller the EIS radius of a sample is, the higher the efficiency of photoelectric separation and migration is. In Fig. 6(c), the Nyquist diagram shows that the arc radius of 12 wt% Ag@ZIF-8/g-C_3N_4 was smaller than those of bare g-C_3N_4 and the other composites. This indicated that the photogenerated carrier transfer resistance of 12 wt% Ag@ZIF-8/g-C_3N_4 was the lowest. The results of EIS were consistent with those of PL. This indicated that 12 wt%

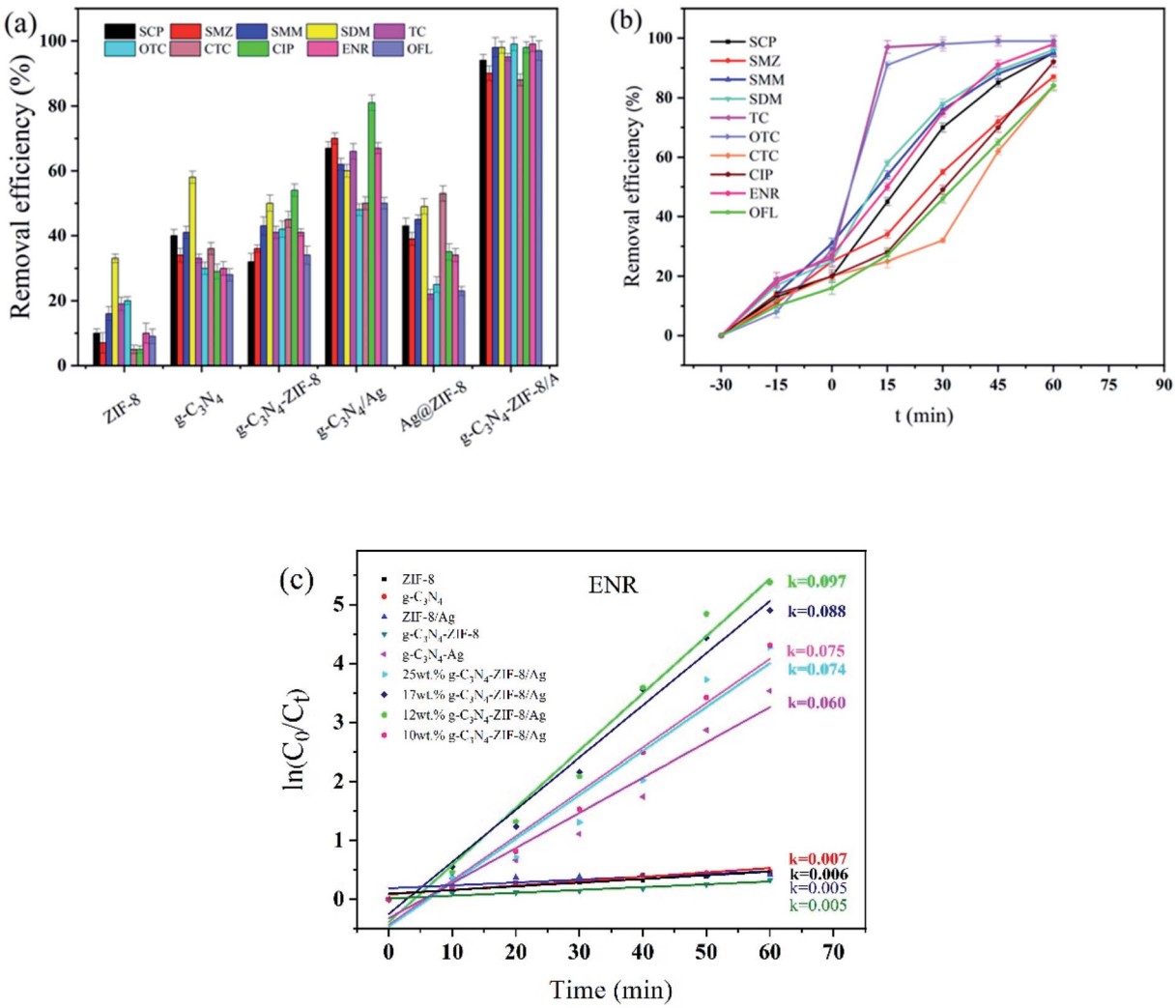

Fig. 7 (a) Degradation of antibiotics by the different materials under visible light irradiation, (b) photocatalytic degradation performance at different times and (c) kinetic linear fitting curves of enrofloxacin under different materials.

Ag@ZIF-8/g-C_3N_4 had a better photoelectric separation efficiency.

3.2 Photocatalytic degradation properties

To evaluate the photocatalytic performance of the prepared products, we carried out photocatalytic degradation tests of 10 antibiotics of 3 categories in aqueous solution under light irradiation. The catalytic reaction system contained ten antibiotics (10 μg ml^{-1} for each), TC, OTC, CTC, CIP, ENR, OFL, SMZ, SDM, SCP and SMM. Before the photocatalysis experiment, we stirred the mixture in the dark for 30 min to reach the adsorption–desorption equilibrium. 12 wt% Ag@ZIF-8/g-C_3N_4 was used as the photocatalyst and the mixture was irradiated for 60 min. We took out 1.0 ml of the suspension and filtered it using a 0.22 mm filter membrane at given time intervals. UHPLC-MS/MS technology was used for the qualitative and quantitative analysis of each target antibiotic. C/C_0 was calculated as the degradation removal rate, where C_0 is the antibiotic concentration after dark adsorption and C is the actual concentration of the antibiotic after the photocatalytic degradation process. The photocatalytic performances of ZIF-8, g-C_3N_4, ZIF-8/g-C_3N_4 and Ag/g-C_3N_4 are shown in Fig. 7(a). The photocatalytic degradation performances at different times are shown in Fig. 7(b). In addition, the photocatalytic degradation abilities of Ag@ZIF-8 and 12 wt% Ag@ZIF-8/g-C_3N_4 were also measured after 60 min under the same conditions. By comparing bare ZIF-8 and g-C_3N_4 with the g-C_3N_4/ZIF-8 composite, ZIF-8, with good adsorption performance, was shown to be almost ineffective at increasing the photocatalytic activity of g-C_3N_4. However, compared with pristine ZIF-8 and g-C_3N_4, as Ag nanoparticles were introduced, Ag/ZIF-8 and Ag/g-C_3N_4 all showed significantly enhanced photoactivity performances under visible light irradiation. Under visible light irradiation (>490 nm), the optimized photocatalyst (12 wt% Ag@ZIF-8/g-C_3N_4) presented the highest photocatalytic activity. The removal rate for each antibiotic selected under visible light irradiation was over 90%. However, the removal efficiencies of all Ag@ZIF-8/g-C_3N_4 composites (10 wt%, 12 wt%, 17 wt%, 25 wt%) were significantly improved, with increased degradation rates of the various multi-residue antibiotics. When the amount of $AgNO_3$ was 1.0 mmol, the 12 wt% Ag@ZIF-8/g-C_3N_4 photocatalyst showed excellent photocatalytic activity. This was because excessive $AgNO_3$ will aggregate on the surface of Ag@ZIF-8/g-C_3N_4, resulting in a reduced photocatalytic performance.

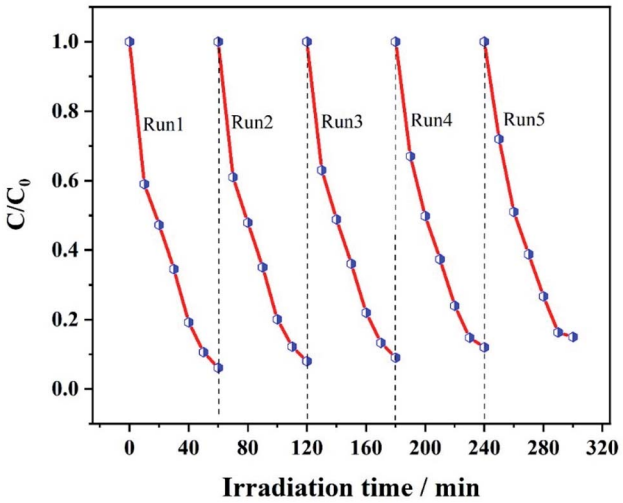

Fig. 8 Cycling experiment of Ag@ZIF-8/g-C_3N_4 for the CIP photocatalytic degradation reaction.

In addition, the degradation kinetics data were fitted using a pseudo first-order model, expressed as: $\ln(C_0/C_t) = K_t$. As shown in Fig. 7(b), the 12 wt% Ag@ZIF-8/g-C_3N_4 composite showed the highest apparent reaction rate constants (ENR $k = 0.097\ min^{-1}$, CIP $k = 0.071\ min^{-1}$, OFL $k = 0.056\ min^{-1}$, SMZ $k = 0.037\ min^{-1}$, SDM $k = 0.056\ min^{-1}$, SCP $k = 0.047\ min^{-1}$, SMM $k = 0.062\ min^{-1}$, TC $k = 0.065\ min^{-1}$, OTC $k = 0.066\ min^{-1}$ and CTC $k = 0.072\ min^{-1}$) compared with those of the other substances. They were 10.1, 13.8, 9.3, 7.4, 7.0, 7.8, 8.9, 13.0, 11.0 and 14.4 times those of pure g-C_3N_4.

Remarkably, compared with other photocatalysts (Table 1), the proposed Ag@ZIF-8/g-C_3N_4 could degrade the most antibiotics in the shortest time with the least catalyst. The results in this study showed an innovative Z-scheme heterojunction photocatalyst capable of efficiently degrading multiple classes of antibiotics under visible-light irradiation.

As requirements for practical applications, the stability and reusability of the catalyst are important. The 12 wt% Ag@ZIF-8/g-C_3N_4 composite for various multi-residue antibiotic degradation was reused five times under the same reaction conditions. As shown in Fig. 8, the Ag@ZIF-8/g-C_3N_4 composite has

Table 1 Summary of photocatalytic degradation by different photocatalysts

Photocatalyst	Light	Dosage	Target	Degradation	Ref.
Ag/AgCl/ZIF-8	500 W, Xe, $\lambda > 400$ nm	50 mg	RhB, 100 ml, 10 ppm	99.12% (90 min)	41
ZIF-8@TiO_2	300 W, Xe, $\lambda > 420$ nm	60 mg	Tc, 100 ml, 100 ppm	90% (120 min)	42
ZIF-8/g-C_3N_4	300 W, Xe, $\lambda > 420$ nm	10 mg	U(VI), 100 ml, 10 ppm	87.5% (120 min)	43
ZIF-8/TiO_2	UV	10 mg	RhB, 30 ml, 10 ppm	87.5% (120 min)	44
			MB, 30 ml, 10 ppm	66% (120 min)	
Ag/AgCl@ZIF-8/g-C_3N_4	150 W, Xe, $\lambda > 420$ nm	50 mg	LVFX, 50 ml, 10 ppm	87.3% (60 min)	45
MoS_2/ZIF-8	300 W, Xe, $\lambda > 420$ nm	20 mg	CIP, 50 ml, 20 ppm	93.2% (180 min)	46
			TC, 50 ml, 20 ppm	75.6% (180 min)	
Ag@ZIF-8/g-C_3N_4	300 W, Xe, $\lambda > 420$ nm	20 mg	Ten antibiotics, 30 ml, 10 ppm	90% (60 min)	This work

excellent stability and reusability. This is because the CIP photodegradation performance of the 12 wt% Ag@ZIF-8/g-C_3N_4 composite did not significantly decay after 5 cycles.

3.3 Main reactive species

Hydroxyl radicals ($^{\bullet}OH$), holes (h^+) and superoxide radicals ($^{\bullet}O_2^-$) are the main reactive species in the process of the photodegradative removal of multi-residue antibiotics. We designed trapping experiments of free radicals and holes to reveal the main active species during the photodegradation using the 12 wt% Ag@ZIF-8/g-C_3N_4 composite as a photocatalyst. We used BQ, EDTA–2Na and IPA as $^{\bullet}O_2^-$, h^+ and $^{\bullet}OH$ scavengers as probes to quantitatively trap radicals in the photocatalytic reaction system. As shown in Fig. 9(a), BQ, IPA and EDTA–2Na were separately added into the reaction system. The degradation efficiencies were reduced upon the addition of BQ and IPA into those systems, while they were almost unchanged for EDTA–2Na. These results indicate that $^{\bullet}O_2^-$ and $^{\bullet}OH$ were the predominant reactive species in the photodegradation systems of 12 wt% Ag@ZIF-8/g-C_3N_4.

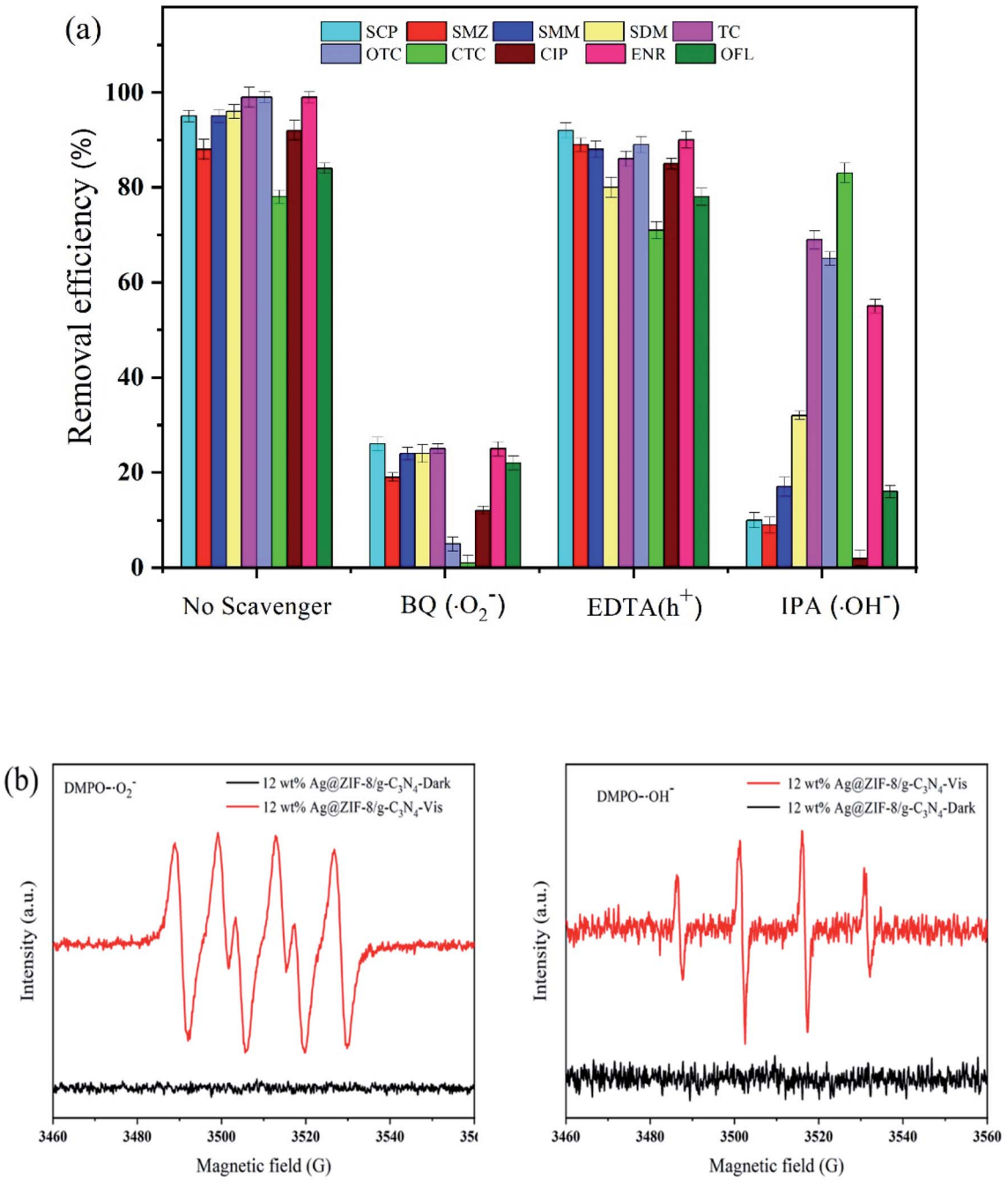

Fig. 9 (a) The effects of scavengers on the photodegradation efficiency of antibiotics in the presence of the Ag@ZIF-8/g-C_3N_4 photocatalyst and (b) ESR spectra of DMPO–$^{\bullet}O_2^-$ and DMPO–$^{\bullet}OH$.

As shown in Fig. 9(b), we measured the electron spin resonance (ESR) spin spectra to further determine these active species ($^{\bullet}O_2^-$ and $^{\bullet}OH$) in the photodegradation systems of the Ag@ZIF-8/g-C_3N_4 composite. In particular, we could easily capture the superoxide radicals ($^{\bullet}O_2^-$) and hydroxyl radicals ($^{\bullet}OH$) produced in the photodegradation system using 5,5-dimethyl-L-pyrroline *N*-oxide (DMPO) in aqueous solution to produce the DMPO–$^{\bullet}OH$ and DMPO–$^{\bullet}O_2^-$ adducts, respectively. As shown in Fig. 9(b), the ESR signals of both the DMPO–$^{\bullet}O_2^-$ and DMPO–$^{\bullet}OH$ adducts can be monitored in the presence of the Ag@ZIF-8/g-C_3N_4 composite after 8 min of visible light irradiation. This indicates that Ag@ZIF-8/g-C_3N_4 can produce the stronger active species $^{\bullet}O_2^-$ and $^{\bullet}OH$. Based on the results, the construction of the heterojunction between Ag@ZIF-8 and g-C_3N_4 can significantly promote the production of $^{\bullet}O_2^-$ and $^{\bullet}OH$ radicals. They are the main reactive species for the degradation of the antibiotic molecules in the photodegradation process.

3.4 Measurement of the photodegradation products

The transformation products of antibiotics were detected by UPLC-MS/MS (using SCP and CIP as examples) during the photocatalytic process. The possible degradation pathways and intermediate products of SCP and CIP are shown in Fig. S1 and S2,† respectively. Two transformation products with *m*/*z* of 251 (M1) and 221 (M2) for SCP (*m*/*z* = 285) were observed, and the corresponding molecular structures are shown in Fig. S1.† Six transformation products with *m*/*z* of 334 (M1), 306 (M2), 263 (M3), 164 (M4), 156 (M5) and 154 (M6) for CIP (*m*/*z* = 332) were observed, and the corresponding molecular structures are shown in Fig. S2.† The photodegradation products for all 10 selected antibiotics can be degraded into CO_2, H_2O and other small, mineralized molecules.

3.5 Photocatalytic mechanism

Based on the M–S plots (Fig. 10(a and b)), the E_{fb} of g-C_3N_4 and ZIF-8 are −1.10 and −0.70 V (*vs.* Ag/AgCl, pH = 7), corresponding to −0.49 and −0.09 V (*vs.* NHE, pH = 7), respectively. Typically, the CB potential of an n-type semiconductor is about 0.2 V greater than that of the E_{fb}. Thus, the E_{CB} of g-C_3N_4 and ZIF-8 are −0.69 and −0.29 V (*vs.* NHE, pH = 7). As shown in Fig. 10(c and d), after doping silver ions into ZIF-8, the band gap of ZIF-8 was reduced from 4.90 to 3.10 eV, because of the defect level above the VB of ZIF-8. Therefore, the VBs of g-C_3N_4 and ZIF-8 were determined to 1.92 and 2.81 V, respectively.

In light of the above analysis and test results, we proposed a potential Z-scheme charge-transfer path and photocatalytic mechanism for the elimination of multiple classes of

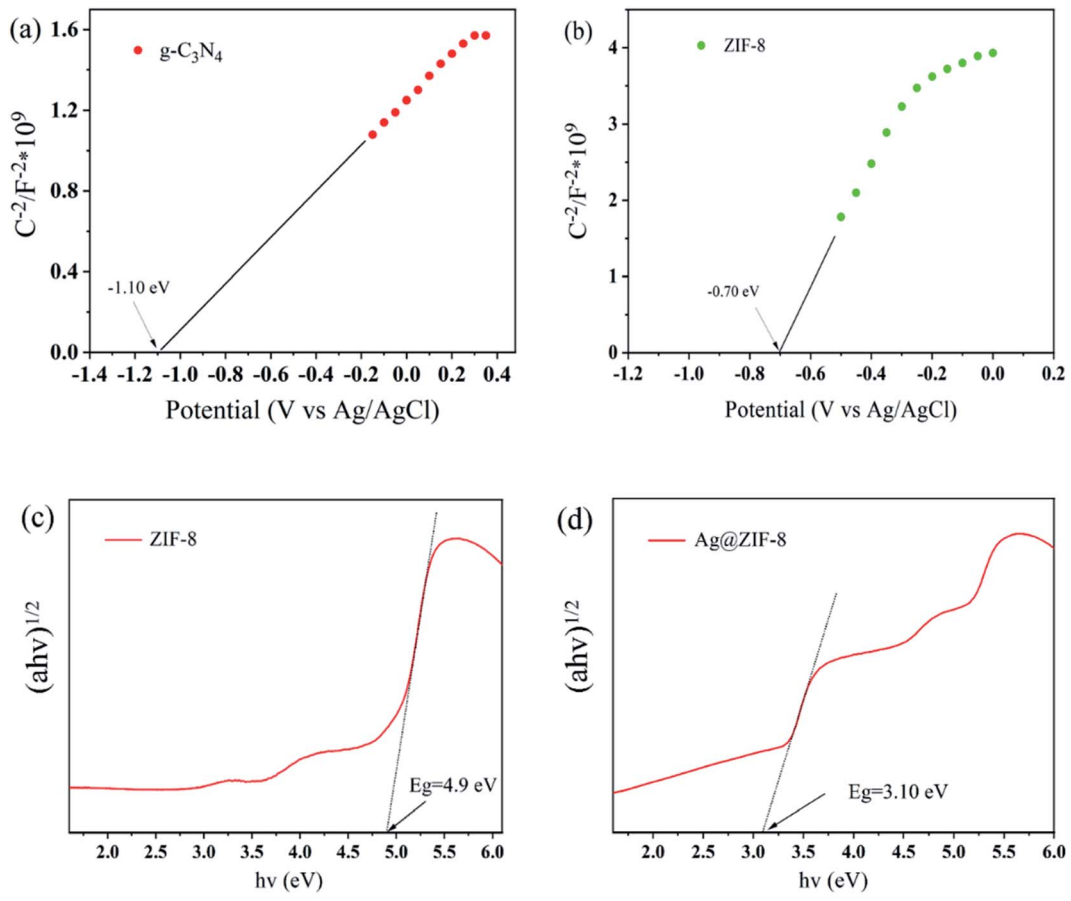

Fig. 10 (a and b) Mott–Schottky (M–S) plots of g-C_3N_4 and ZIF-8, respectively. (c and d) Plot of $(ahv)^{1/2}$ *versus* energy for ZIF-8 and Ag@ZIF-8, respectively.

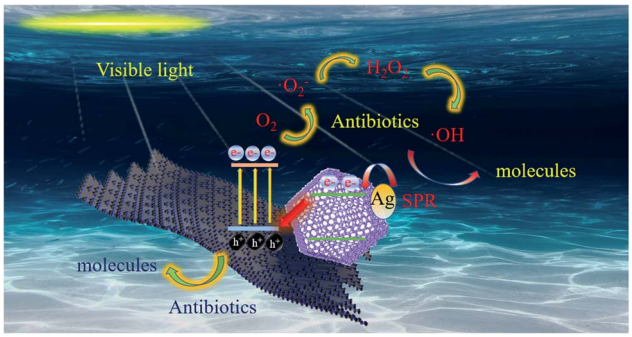

Fig. 11 Proposed photocatalysis mechanism of the Ag@ZIF-8/g-C_3N_4 Z-scheme heterojunction.

antibiotics over the Ag@ZIF-8/g-C_3N_4 heterostructure under visible light irradiation (Fig. 11).

When g-C_3N_4 and Ag@ZIF-8 are in close contact, the charges are redistributed to reach the equilibrium of E_f levels. As a result, a built-in electric field directed from g-C_3N_4 to ZIF-8 is generated at the interface between the two. Meanwhile, the *in situ* generated Ag NPs have enough energy to surmount the Schottky barrier at the Ag@ZIF-8 interface and readily transfer to the CB of ZIF-8, and recombine with h^+ on g-C_3N_4 under the built-in electric field. This provides evidence for Z-scheme charge transfer.

We used the shift of the binding energy in the XPS spectra to demonstrate the electron migration pathway for a direct Z-scheme photocatalyst. Compared with those of Ag@ZIF-8 (Fig. 5(d)), the Zn 2p states of Ag@ZIF-8/g-C_3N_4 were negatively shifted. This indicates that the electrons transfer from Ag@ZIF-8 to g-C_3N_4. Obviously, the charge-carrier migration mechanism of the Ag@ZIF-8/g-C_3N_4 direct Z-scheme photocatalyst was demonstrated by the noble metal loading and *in situ* XPS evaluation. In addition, the prepared 12 wt% Ag@ZIF-8/g-C_3N_4 showed the best photocatalytic degradation activity for multi-residue antibiotics because of its sufficient reduction potential (Fig. 7(a)). All the prepared composites showed better photocatalytic degradation efficiency (different silver nitrate addition amounts (Fig. S4†) and different mass ratios (Fig. S5†)). The efficient removal of multi-residue antibiotics is attributed to the structure of the direct Z-scheme heterojunction between Ag@ZIF-8 and g-C_3N_4.

In addition, ESR test results further confirmed the above results. According to the energy band position, electron-rich Ag@ZIF-8 cannot produce $^{\bullet}O_2^-$, because its CB position is more positive compared to the potential of $O_2/^{\bullet}O_2^-$ (−0.33 V *vs.* NHE), and g-C_3N_4 cannot generate $^{\bullet}OH$, because its VB position is more negative than the potential of $H_2O/^{\bullet}OH$ (2.40 V *vs.* NHE). However, $^{\bullet}OH$ signals and $^{\bullet}O_2^-$ signals were detected for the composite, indicating that the charge transfer mode follows a Z-scheme mechanism rather than the traditional type II.

4. Conclusions

In conclusion, by combining the catalytic properties of Ag nanoparticles and the molecular sieving and orientation effects of ZIF-8, the Ag@ZIF-8/g-C_3N_4 composite with a direct Z-scheme heterojunction was successfully prepared through a simple method. Using a range of characterization techniques, we investigated the morphology, chemical composition, and optical properties of the prepared samples by SEM, HRTEM, XRD, FTIR, UV-vis DRS, and photoluminescence techniques. The PL and EIS tests, as well as the UV-vis DRS test, proved that Ag, ZIF-8 and g-C_3N_4 had suitable band gaps that provided structures for the establishment of a Z-scheme heterojunction. Under visible light irradiation, the 12 wt% Ag@ZIF-8/g-C_3N_4 composite exhibited the highest photocatalytic performance for 10 antibiotics in 3 categories. The removal rates of the selected antibiotics were all over 90% under visible light illumination. Their average apparent reaction rates were 10.27 times that of pure g-C_3N_4. This further proved that the direct Z-scheme photocatalytic mechanism could significantly enhance the visible light absorption and e^-–h^+ separation efficiency. Through ESR tests, we found that Ag@ZIF-8/g-C_3N_4 could produce the stronger active species of $^{\bullet}O_2^-$ and $^{\bullet}OH$ radicals. This further confirmed the successful construction of the direct Z-scheme heterojunction. Therefore, this study prepared a Z-scheme photocatalyst by the integration of adsorption and photocatalytic degradation for antibiotic removal in ambient water, which is considered as a promising strategy.

Conflicts of interest

The authors declare that they have no competing interests.

References

1 X. W. Liu, K. Lv, C. X. Deng, Z. M. Yu, J. H. Shi and A. C. Johnson, *Environ. Pollut.*, 2019, **252**, 1532–1538.
2 S. Zhong, J. J. Yang, H. Zhou, C. Y. Li and L. Bai, *Sol. Energy Mater. Sol. Cells*, 2022, **238**, 111646.
3 Y. Li, K. Yin, L. L. Wang, X. L. Lu, Y. Q. Zhang, Y. T. Liu, D. F. Yan, Y. Z. Song and S. L. Luo, *Appl. Catal., B*, 2018, **239**, 537–544.
4 T. Takata and K. Domen, *ACS Energy Lett.*, 2019, **4**, 542–549.
5 K. Yu, H. B. Huang, J. T. Wang, G. F. Liu, Z. Zhong, Y. F. Li, H. L. Cao, J. Lv and R. Cao, *J. Mater. Chem. A*, 2021, **9**, 7759.
6 Y. J. Ren, D. Q. Zeng and W.-J. Ong, *Chin. J. Catal.*, 2019, **40**, 289–319.
7 J. W. Fu, J. G. Yu, C. J. Jiang and B. Cheng, *Adv. Energy Mater.*, 2018, **8**, 1701503.
8 Q. Hao, T. Chen, R. T. Wang, J. R. Feng and D. M. Chen, *J. Clean. Prod.*, 2018, **197**, 1222–1230.
9 A. S. Mestre and A. P. Carvalho, *Molecules*, 2019, **24**, 3702.
10 Y. Chen, Z. X. Fan, Z. C. Zhang, W. X. Niu, C. L. Li, N. L. Yang and B. Chen, *Chem. Rev.*, 2018, **118**, 6409–6455.
11 J. X. Low, C. J. Jiang, B. Chen, S. Wageh, A. A. Al-Ghamdi and J. G. Yu, *Small Methods*, 2017, **1**, 1700080.
12 Q. L. Xu, L. Y. Zhang, J. G. Yu, S. Wageh, A. A. Al-Ghamdi and M. Jaroniec, *Mater. Today*, 2018, **21**, 1042–1063.
13 W. H. Zhang, A. R. Mohamed and W.-J. Ong, *Angew. Chem., Int. Ed.*, 2020, **59**, 22894–22915.

14 D. L. Huang, S. Chen, G. M. Zeng, X. M. Gong, C. Y. Zhou, M. Cheng, W. J. Xue and J. Li, *Coord. Chem. Rev.*, 2019, **385**, 44–80.
15 W. L. Yu, D. F. Xu and T. Y. Peng, *J. Mater. Chem. A*, 2015, **3**, 19936–19947.
16 S. W. Liu, F. Chen, S. T. Li, X. X. Peng and Y. Xiong, *Appl. Catal., B*, 2017, **211**, 1–10.
17 X. Q. Hao, J. Zhou, Z. W. Cui, Y. C. Wang, Y. Wang and Z. G. Zou, *Appl. Catal., B*, 2018, **229**, 41–51.
18 G. Gebreslassie, P. Bharali, U. Chandra, A. Sergawie, P. K. Boruah, M. R. Das and E. Alemayehu, *J. Photochem. Photobiol., A*, 2019, **382**, 111960.
19 J. Wu, J. Y. Hu, H. H. Qian, J. J. Li, R. Yang and L. B. Qu, *Diamond Relat. Mater.*, 2022, **121**, 108738.
20 Z. J. Qu, Z. Y. Jing, X. M. Chen, Z. X. Wang, H. F. Ren and L. H. Huang, *J. Environ. Sci.*, 2023, **125**, 349–361.
21 G. Gebreslassie, P. Bharali, U. Chandra, A. Sergawie, P. K. Boruah, M. R. Das and E. Alemayehu, *Appl. Organomet. Chem.*, 2019, **33**, e5002.
22 L. F. Cui, X. Ding, Y. G. Wang, H. C. Shi, L. H. Huang and Y. H. Zuo, *Appl. Surf. Sci.*, 2017, **391**, 202–210.
23 Y. Q. Zhang, Y. M. Sun, Y. Man, H. Yang, R. Y. Zhao, G. Q. Xiang, X. M. Jiang, L. J. He and S. S. Zhang, *Chem. Eng. J.*, 2022, **440**, 135723.
24 Y. F. Wang, W. Zhao, Z. Y. Qi, L. Zhang, Y. N. Zhang, H. O. Huang and Y. Z. Peng, *Chem. Eng. J.*, 2020, **394**, 124992.
25 G. Y. Liu, L. Y. Li, D. H. Xu, X. D. Huang, X. M. Xu, S. N. Zheng, Y. G. Zhang and H. Lin, *Carbohydr. Polym.*, 2017, **175**, 584–591.
26 H. Dai, X. Z. Yuan, L. B. Jiang, H. Wang, J. Zhang, J. J. Zhang and T. Xiong, *Coord. Chem. Rev.*, 2021, **441**, 213985.
27 Z. L. Wang, X. Y. Chen, Z. Meng, M. X. Zhao and H. J. Zhan, *Water Sci. Technol.*, 2020, **82**, 2322–2336.
28 C. C. Hu, Y. C. Huang, A. L. Chang and M. Nomura, *J. Colloid Interface Sci.*, 2019, **553**, 372–381.
29 P. Y. Jiang, K. F. Yu, H. B. Yuan, R. He, M. P. Sun, F. Tao, L. B. Wang and W. K. Zhu, *J. Mater. Chem. A*, 2021, **9**, 9809.
30 S. J. Li, C. C. Wang, Y. P. Liu, B. Xue, W. Jiang, Y. Liu, L. Y. Mo and X. B. Chen, *Chem. Eng. J.*, 2021, **415**, 128991.
31 N. Chang, Y. R. Chen, F. Xie, Y. P. Liu and H. T. Wang, *Colloids Surf., A*, 2021, **616**, 126351.
32 G. D. Fan, X. M. Zheng, J. Luo, H. P. Peng, H. Lin, M. C. Bao, L. Hong and J. J. Zhou, *Chem. Eng. J.*, 2018, **351**, 782–790.
33 S. W. Liu, F. Chen, S. T. Li, X. X. Peng and Y. Xiong, *Appl. Catal., B*, 2017, **211**, 1–10.
34 J. L. Shi, L. N. Zhang, N. N. Sun, D. Hu, Q. Shen, F. Mao, Q. Gao and W. Wei, *ACS Appl. Mater. Interfaces*, 2019, **11**, 28858–28867.
35 C. H. Liu, H. L. Dai, C. Q. Tan, Q. Y. Pan, F. P. Hu and X. M. Peng, *Appl. Catal., B*, 2022, **310**, 121326.
36 X. Meng, C. Duan, Y. L. Zhang, W. L. Lu, W. L. Wang and Y. H. Ni, *Compos. Sci. Technol.*, 2020, **200**, 108384.
37 D. S. Yuan, J. Ding, J. Zhou, L. Wang, H. Wan and W. L. Dai, *J. Alloys Compd.*, 2018, **762**, 98–108.
38 H. Zhang, G. Wang, D. Chen, X. J. Lv and J. H. Li, *Chem. Mater.*, 2008, **20**, 6543–6549.
39 W. Li, X. Wang, M. Li, S. A. He, Q. Ma and X. C. Wang, *Appl. Catal., B*, 2020, **268**, 118384.
40 N. Q. Thang, A. Sabbah, L. C. Chen, K. H. Chen, C. M. Thi and P. V. Viet, *Chemosphere*, 2021, **282**, 130971.
41 G. H. Zuo, A. Q. Wang, Y. Yang, H. L. Huang, F. B. Wang, H. W. Jiang, L. Zhang and Y. J. Zheng, *J. Porous Mater.*, 2020, **27**, 339–345.
42 R. Li, W. Li, C. Jin, Q. Y. He and Y. Z. Wang, *J. Alloys Compd.*, 2020, **825**, 154008.
43 M. Q. Qiu, Z. X. Liu, S. Q. Wang and B. W. Hu, *Environ. Res.*, 2021, **196**, 110349.
44 R. Chandra, S. Mukhopadhyay and M. Nath, *Mater. Lett.*, 2016, **164**, 571–574.
45 J. B. Zhou, W. Liu and W. Q. Cai, *Sci. Total Environ.*, 2019, **696**, 133962.
46 W. Q. Chen, L. Y. Li, W. H. Qiu, L. Tang, L. Xu, K. J. Xu and M. H. Wu, *Engineering*, 2019, **5**, 755–767.